Methodology to determine the coupling of continental clouds with surface and boundary layer height under cloudy conditions from lidar and meteorological data

Tianning Su[1], Youtong ~~Zheng[1]~~Zheng[2], and Zhanqing Li[1]

[1]Department of Atmospheric and Oceanic Sciences & ESSIC, University of Maryland, College Park, Maryland 20740, USA

[2]The Program in Atmospheric and Oceanic Sciences, Princeton University, and NOAA/Geophysical Fluid Dynamics Laboratory, Princeton, NJ, USA

Correspondence to: zhanqing@umd.edu; tianning@umd.edu

Abstract

The state of coupling between clouds and surface or boundary-layer have been investigated much more extensively for marine stratocumulus clouds than for continental low clouds, partly due to more complex thermodynamic structures over land. A manifestation is a lack of robust remote sensing methods to identify coupled and decoupled clouds over land. Here, we have generalized the concept of coupling and decoupling to low clouds over land, based on potential temperature profiles. Furthermore, by using ample measurements from a lidar and a suite of surface meteorological instruments at the U.S. Department of Energy's Atmospheric Radiation Measurement Program's Southern Great Plains site from 1998 to 2019, we have developed a method to simultaneously retrieve the planetary boundary layer (PBL) height (PBLH) and coupled states under cloudy conditions during the daytime. The coupled states derived from lidar show strong consistency with those derived from radiosondes. Retrieving the PBLH under cloudy conditions that has been a persistent problem in lidar remote sensing, is resolved in this study. Our method can lead to high-quality retrievals of the PBLH under cloudy conditions, and the determination of cloud coupling states. With the new method, we find that coupled clouds are sensitive to changes in the PBL, with a strong diurnal cycle whereas decoupled clouds and the PBL are weakly related. Since coupled and decoupled clouds have distinct features, our new method offers an advanced tool to separately investigate them in climate systems.

1 Introduction

A large fraction of low clouds is driven by surface fluxes through the conduits of the planetary boundary layer (PBL) over land (e.g., Betts, 2009; Ek and Holtslag, 2004; Golaz et al., 2002; Teixeira and Hogan, 2002; Zheng et al., 2020; Wei et al., 2020; Santanello et al., 2018). This is a coupled cloud-surface system (Cheruy et al., 2014; Zheng &and Rosenfeld, 2015; Wu et al., 1998). However, not all low clouds respond to surface forcing. Those clouds without close interactions with the local surface are considered to be in a decoupled state. Given that the PBL is, by definition, the lowest atmospheric layer influenced by the underlying surface (Stull, 1988), to what degree the PBL top overlaps with cloud bases becomes a good criterion to separate coupled and decoupled low clouds.

Conventionally, the "coupled state" of a cloud-topped marine boundary layer implies that the moist conserved variables are vertically well mixed within the PBL (Bretherton and Wyant, 1997; Dong et al., 2015; Zheng &and Li, 2019; Zheng et al., 2018). However, such a definition cannot be simply applied to clouds over land since the moist conserved variables typically show considerable variations due to the relatively complex thermodynamics (Driedonks, 1982; Stull, 1988). The definition and the determination methods of the PBL over land also widely differ from those over ocean (Garratt, 1994; Vogelezang &and Holtslag, 1996). The concept of coupled and decoupled states is typically used to characterize marine stratocumulus clouds due to their large-scale coverages (Nicholls, 1984). Since stratocumulus only constitutes a relatively small portion of continental clouds (Warren et al., 1986), we attempt to extend

3

61 the concept of coupling and decoupling to characterize low clouds over land.

62   Following parcel theory, the lifted condensation level (LCL) has been used to

63 diagnose a coupled cloud, based on the distance between the LCL and the cloud base

64 (e.g., Dong et al., 2015; Glenn et al., 2020; Zheng ~~&~~and Rosenfeld, 2015; Zheng et al.,

65 2020). When potential temperature and humidity are uniformly distributed in the

66 vertical, the LCL should be consistent with the cloud base for coupled cases. However,

67 the cloud base for coupled cases can considerably differ from the LCL over land

68 because potential temperature and humidity have large variabilities in the vertical scale

69 within the PBL over land (Guo et al., 2016; Stull, 1988; Su et al., 2017a). Therefore, a

70 robust remote sensing method is still warranted to distinguish coupled and decoupled

71 clouds over land.

72   Since the PBL height (PBLH) is the maximum height directly influenced by surface

73 fluxes, we consider coupling with the PBL equivalent to coupling with the land surface.

74 Thus, we use the PBLH as a critical parameter to diagnose the coupling between clouds

75 and the land surface. The degree of coupling may thus be gauged in terms of

76 quantitative differences between the cloud base and the PBL top. Such differences can

77 be determined in a height coordinate system or in a potential temperature coordinate

78 system (Kasahara, 1974). For this purpose, ground-based lidar has great potential

79 because it can continuously track the development of the PBL (Demoz et al., 2006;

80 Hageli et al., 2000; Sawyer ~~&~~and Li, 2013; Su et al., 2017b) and clouds (Clothiaux et

81 al., 2000; Platt et al., 1994; Zhao et al., 2014) at high temporal and vertical resolutions.

82   By jointly using lidar measurements and meteorological data from the U.S.

83 Department of Energy's Atmospheric Radiation Measurement (ARM) Southern Great

84 Plains (SGP) site (36.6°N, 97.48°W), we attempt to identify coupled and decoupled low

85 clouds during the daytime. Unlike previous studies that use the LCL or radiosonde (RS)

86 data to diagnose coupled clouds (e.g., Dong et al., 2015; Zheng ~~&~~and Rosenfeld, 2015),

87 this study provides the first lidar-based method to automatically determine the coupling

88 and decoupling of low clouds over land at a high temporal resolution.

89   The paper is organized as follows. Section 2 describes the measurements and data.

90 Section 3 describes the new methodology in terms of the definition and implementation.

91 The performance of the method is demonstrated in Section 4, and a summary is

92 presented in Section 5.

93

94 **2   Data Descriptions**

95 *2.1 Radiosonde*

96   RS launches took place at least four times per day at the ARM SGP site, usually at

97 0030, 0630, 1230, and 1830 local time (LT). Holdridge et al. (2011) provide technical

98 details about the ARM RS (https://www.arm.gov/capabilities/instruments/sonde). In

99 this study, we consistently use daylight saving time (Coordinated Universal Time -5 h)

100 as local time throughout the year to avoid inconsistencies between summer and winter.

101 Besides the routine measurements, there are fewer, but still considerable numbers of

102 RS data obtained at other times of the day (e.g., 0930, 1200, 1300, 1530, and 1900 LT).

103 These supplemental RS samples at other times comprise ~10% of the total number of

104 cases. RS data from 0630–1900 LT are utilized in this study. The vertical resolution of

105 RS data varies according to the rising rate of the balloon, but measurements are

106 generally taken ~10 m apart. We further vertically average the RS data to achieve a

107 vertical resolution of 5 hPa.

108 There are several methods to determine PBLH from RS-measured temperature,

109 pressure, and humidity profiles. Theyse methods include, among others, the parcel

110 method (Holzworth, 1964), the gradient methods (Stull, 1988; Seidel et al., 2010), and

111 the Richardson number method (Vogelezang and Holtslag, 1996). After

112 examiningBased on the previous methods, Liu and Liang. (2010) useproposed a

113 different strategiesapproach to determine the PBLH that is valid under different

114 thermodynamics stability conditions. The As this method demonstrates rRrobust

115 performance was demonstrated over the SGP site and in other major field campaign

116 sites itsaround the world (Liu and Liang, 2010). Thus, we adopted this method which

117 was thus chosento calculate PBLH from RS data in ourthis study. By using the well-

118 established method developed by Liu and Liang (2010), we retrieved PBLHs over the

119 SGP site from RS measurements. The potential temperature is corrected as the virtual

120 potential temperature, θ_v, using the water vapor mixing ratio [WVMR; θ_v = (1 +

121 0.61 WVMR)]. The virtual potential temperature does not include a correction for the

122 liquid water content profile, as this is challenging to measure in many conditions.

123 Therefore, the virtual potential temperature is not conserved during moist convection.

124 Since we mainly focus on the sub-cloud atmosphere, this is not a serious problem.

125 Moreover, we use scaled RS moisture profiles normalized by the total precipitable

Formatted: Font: Not Bold

126 water   vapor   derived   from   the   microwave   radiometer

127 (https://www.arm.gov/capabilities/vaps/lssonde, Revercomb et al., 2003).

128

129 *2.2 Micropulse lidar (MPL) system*

130 MPL backscatter profiles were collected at the SGP site from September 1998 to

131 July 2019 with high continuity (Campbell et al., 2002). Technical details and data

132 availability   can   be   found   at   the   website

133 https://www.arm.gov/capabilities/instruments/mpl. The backscatter profiles have a

134 vertical resolution of 30 m. MPL signals have an initial temporal resolution of 10–30 s

135 and are averaged every 10 min for this study. Due to the inherent problem of lidar

136 observations, there is a ~0.2-km near-surface "blind zone". Following the standard

137 lidar-data processing, background subtraction, signal saturation and overlapping, after-

138 pulse and range corrections are applied to the raw MPL data (Campbell et al., 2002,

139 2003). Questionable data are excluded based on the quality-control flags.

140

141 *2.3 Cloud product*

142 The MPL can be used to detect cloud layers based on signal gradients (Platt et al.,

143 1994). Lidar-based methods are accurate for determining the cloud-base height (CBH)

144 but may miss information about the cloud top due to the signal saturation within an

145 optically thick cloud (Clothiaux et al., 2000). Under this condition, the cloud radar

146 provides a better estimation of the cloud-top height (CTH). In this study, we directly

147 use an existing quality-controlled cloud product, CLDTYPE/ARSCL

148 (https://www.arm.gov/capabilities/vaps/cldtype), which combines information from

149 the MPL, ceilometer, and cloud radar to determine the vertical boundaries of clouds

150 (Clothiaux et al., 2000; Flynn et al., 2017). For the lowest cloud base, the best

151 estimation from laser-based techniques (i.e., MPL and ceilometer) is used. The original

152 temporal resolution of the CLDTYPE/ARSCL product is 1 min, averaged to a 10-min

153 temporal resolution. To avoid averaging jumps in signal between different clouds, a

154 cloud is considered to be continuous if its base height varies less than 0.25 km between

155 two consecutive profiles.

156

157 **3 Methodology**

158 *3.1 Definition of coupled and decoupled clouds based on thermodynamics*

159 The definition of the state of cloud-surface coupling over land is a critical question.

160 For marine stratocumulus, coupled clouds are identified when the liquid water potential

161 temperature varies less than a certain threshold (i.e., 0.5 K) below the cloud base (Jones

162 et al., 2011). We try to extend the concept of coupling and decoupling to clouds over

163 land. The PBL over land is typically buoyancy driven and controlled by surface fluxes

164 during the daytime. We consider a cloud is in the coupled state when it strongly interacts

165 with the buoyancy fluxes within the PBL.

166 Figure 1 presents the idealized vertical profiles of virtual potential temperature (θ_v)

167 under the clear-sky, coupled cloud, and decoupled cloud. A superadiabatic surface layer

8

168   exchanges the heat fluxes between the surface and PBL. The outer layer and

169   entrainment zone are turbulently coupled with the surface, and thus, are considered as

170   the coupled regime. Meanwhile, the free atmosphere is considered as the decoupled

171   regime. Theoretically, θ_v is constant in the outer layer, and follows the wet adiabatic

172   lapse rate in the cloud layer. Although the profiles of θ_v in the real atmosphere can

173   largely differ from the idealized profiles, the relative position between the cloud layer

174   and capping inversion of entrainment zone is clear. For the coupled cases, the cloud

175   base is below the capping inversion of entrainment zone. For the decoupled cases, the

176   cloud base is above the capping inversion. Based on this feature, we can use the virtual

177   potential temperature profiles to diagnose the coupling state of low clouds.

178   We first look at several examples of profiles of θ_v and WVMR from the RS

179   (Figure 2). If the CBH is lower than the PBLH, the cloud is affected by turbulence and

180   buoyancy fluxes in the PBL, such as the cases shown in Figure 2a. Note that the PBLH

181   is not an absolute boundary limiting turbulence and buoyancy fluxes. Due to the

182   overshooting of rising air parcels, we use a range to screen the condition of coupled

183   clouds. As shown in Figure 2b, even when the CBH is slightly above the PBLH,

184   WVMR and θ_v are still relatively consistent between the cloud layer and the PBL and

185   show large step signals at the cloud top.

186   Figure 2c-d shows a clear inversion layer between the cloud base and the PBL top,

187   and the difference in θ_v between the CBH and the PBLH ($\Delta\theta_v$) is relatively large.

188   Such a notable inversion layer prevents the buoyancy fluxes within the PBL from

189   reaching the cloud base, leading to the decoupling between the cloud and the PBL.

9

190 Overall, whether there is a clear inversion between the cloud base and the PBL top is

191 the key factor in determining coupling and decoupling. In this aspect, $\Delta\theta_v$ is the key

192 factor. In Figure 2, $\Delta\theta_v$ for coupled cases (a-c) is -0.32 K and 0.31 K, respectively,

193 and $\Delta\theta_v$ for decoupled cases (d-e) is 1.47 K and 5.0 K, respectively.

194 Therefore, instead of giving a height range to limit the differences between CBH

195 and PBLH, we consider using the differences in θ_v between CBH and PBLH ~~($\Delta\theta_v =$~~

196 ~~$\theta_v^{CBH} - \theta_v^{PBLH}$) to~~ determine the threshold for distinguishing coupled and decoupled

197 clouds. For convenience, we use $\Delta\theta_v$ to refer to the difference in θ_v between the

198 CBH and the PBLH $(\Delta\theta_v = \theta_v^{CBH} - \theta_v^{PBLH})$. For decoupled cases, the cloud base is

199 above the capping inversion of entrainment zone. There is a notable inversion in θ_v

200 between PBL top and decoupled cloud base. Thus, we identify the cases satisfying

201 $\Delta\theta_v > \delta_s$ as being in a decoupled state. Correspondingly, we identify the cases

202 satisfying $\Delta\theta_v < \delta_s$ as being in a coupled state. We set the range of CBH to between

203 0 and 4 km and excluded cases of deep convection (i.e., CBH < 4 km and CTH > 6.5

204 km).

205 As the basic framework of PBL, the slab model assumes that θ_v is constant within

206 the PBL (Wallace and Hobbs, 2006). Under this assumption, δ_s can be set as 0.

207 However, there are certain variations in θ_v within the PBL, which can cause inversions

208 with relatively small magnitudes between the cloud base and PBL top. Figure 3a

209 presents the inversion strength in θ_v within PBL during the daytime. Specifically,

210 inversions represent the layers with continuously increased structures of θ_v. For an

211 inversion layer, the inversion strength is calculated as the differences in θ_v between the

10

212 ~~layer~~ top and bottom of the layer. The inversions near surface or across the PBL top are

213 excluded. Besides the capping inversion and surface inversion, the inversion strength

214 within PBL is typically below 1K. Therefore, we set δ_s as 1 K, which is the same as

215 the criterion for determining stable or convective conditions (Liu ~~&~~and Liang, 2010).

216 Furthermore, we demonstrate the probability density function (PDF) of $\Delta\theta_v$ for the

217 low cloud cases. Coupled and decoupled clouds are classified by the threshold of δ_s

218 (1 K). Through the development of PBL, boundary layer clouds frequently occur in the

219 entrainment zone, and form a coupled cloud-PBL system. For such coupled systems,

220 θ_v at cloud top and PBL top is highly consistent for the majority of cases. Thus, the

221 PDF of $\Delta\theta_v$ shows significantly high values for the range of -2 K to 0.5 K in the

222 coupled regime. Meanwhile, the PDF of $\Delta\theta_v$ is evenly distributed in the decoupled

223 regime. Since we only analyze low clouds, the PDF of $\Delta\theta_v$ slowly decrease when $\Delta\theta_v$

224 is above 10 K.

225 Based on the variations in θ_v within PBL, we set δ_s as 1 K. However, it should

226 note that it is not an absolute value. A similar threshold of 0.5 K has been used for

227 marine stratocumulus (Jones et al., 2011; Dong et al., 2015). Comparing to the marine

228 condition, θ_v show greater variabilities over land. Hence, the threshold is

229 correspondingly larger. On the other hand, since the threshold of 1 K is in the low PDF

230 regime (Figure 3b), the small changes in this value would not notably affect the

231 identifications. Specifically, a 0.1 K difference in δ_s will lead to a 0.5% difference in

232 the identification of coupled cloud.

233 Same to the previous studies (Jones et al., 2010; Dong et al., 2015; Zheng and

11

234 Rosenfeld, 2015), ~~our study~~we identified the coupled clouds as the thermodynamics

235 coupling between surface and cloud base. However, it is an open question whether the

236 entire cloud layer is coupled for coupled cases. It depends on whether the liquid water

237 potential temperature is conserved within the cloud layer, which represents ~~the~~a

238 moisture adiabatic process. This issue is closely related to the cloud types. In the cloud

239 parameterizations, the entire stratocumulus layer is considered to be well-mixed,

240 ~~mean~~while~~,~~ the cumulus-capped layer is usually partially mixed (Lock, 2000). For

241 stratocumulus clouds, the entire cloud layer and PBL are typically fully coupled with

242 surface, when the cloud base is coupled with surface. For the cumulus-capped PBL, the

243 entire cloud layer may not be completely coupled, despite the coupling between cloud

244 base and surface. ~~For stratocumulus clouds, may. Forclouds, they are~~The well-

245 established parameterizations ~~also~~ are supported by many observational studies (e.g.,

246 Betts, 1986; Storer et al., 2015; Berkes et al., 2016, de Roode and Wang. 2006; Ott et

247 al., 2009).

248

249 ~~Following the traditional definition of buoyancy forces (Wallace & Hobbs, 2006), we~~

250 ~~further integrate the buoyancy forces within the lowest 1 km ($-g \int_0^{1km} \frac{1}{\theta} \frac{\Delta\theta}{\Delta z} dz$). Figure~~

251 ~~4 shows the relationships between CBH and buoyancy forces in the lower atmosphere~~

252 ~~for $\Delta\theta_v < \delta_s$ (coupled state) and $\Delta\theta_v > \delta_s$ (decoupled state). In terms of the~~

253 ~~responses to buoyancy forces, dramatic differences between coupled and decoupled~~

254 ~~clouds are seen. Following our previous study (Su et al., 2018), we use the inverse~~

255 ~~fitting ($f(x) = \frac{A}{x} + B$) with consideration of density to establish the relationship~~

12

256 ~~between CBH and buoyancy forces. The magnitude of the correlation coefficient ($R^{\pm}$)~~

257 ~~is designed to measure the degree to which the data fit an inverse relationship. For a~~

258 ~~coupled cloud, changes in CBH to variable buoyancy forces mostly follow an inverse~~

259 ~~function. For the coupled cases, strong buoyancy forces are associated with a thick PBL~~

260 ~~and high CBH. Since a decoupled cloud occurs in the free atmosphere, the CBH of a~~

261 ~~decoupled cloud has a very weak linkage with the buoyancy forces.~~

262

263 *3.2 Lidar-based method to identify coupled and decoupled clouds*

264 *3.2.1 Method description*

265 Given the rapid change in clouds over land, RS observations have limitations when

266 it comes to tracking cloud development due to the coarse temporal resolution and

267 drifting of the balloon. We thus further developed a lidar-based method to identify the

268 coupled states of clouds based on our new algorithm for retrieving the PBLH that can

269 better track the diurnal variations in PBLH than conventional lidar-based approaches

270 (Su et al., 2020). We adapted this algorithm for retrieving the PBLH and developed a

271 new scheme to deal with cloudy conditions. Following the original method (Su et al.

272 2020), the rainy cases are eliminated in the quality control process~~. As stated in Su et~~

273 ~~al. (2020), the rainy cases are eliminated in the quality control process~~. The principles

274 behind the PBLH algorithm are stated next for completeness.

275 Our new PBLH algorithm can retrieve the PBL variability from the MPL under

276 Different Thermo-Dynamic Stability (thus named the DTDS algorithm) conditions,

277   taking into account the vertical coherence and temporal continuity of the PBLH. First,

278   we identify the local maximum positions (LMPs; range: 0.25–4 km) in profiles of the

279   wavelet covariance transform function derived from lidar backscatter (Brooks, 2003).

280   These LMPs are the potential positions of the PBLH. We can use the PBLH derived

281   from morning RS soundings as the starting point. Without morning RS soundings, the

282   algorithm can still work well, with the lowest LMPs selected as the starting point, which

283   reduces by 0.02–0.05 the correlation coefficient between MPL-derived and RS-derived

284   PBLHs (Su et al., 2020).

285   To ensure good continuity, we select the closest LMP to the earlier position of the

286   PBLH. Different stages of PBL development are considered. DTDS-derived PBLHs

287   likely increase during the growth stage and decrease during the decaying stage, but the

288   algorithm is also able to identify decreases during the growth stage or increases during

289   the decaying stage based on the selection scheme described by Su et al. (2020). There

290   are multiple step signals in the backscatter profiles when complex aerosol structures

291   (e.g., the residual layer) are present, leading to multiple LMPs. Based on temporal

292   continuity, we select the appropriate LMP as the position of the PBL top. However,

293   PBLH retrievals still suffer from relatively low accuracies under stable conditions

294   because of the weak vertical mixing and residual layer.

295   Clouds induce strong step signals in the lidar backscatter, further considerably

296   affecting PBLH retrievals. Su et al. (2020) only considered cases where the low cloud

297   top coincided with the previous PBL top, excluding other low-cloud cases (> 60% of

298   all low-cloud cases). Here, we specifically consider coupled and decoupled states of

14

299 low clouds. Due to the MPL's ~0.2-km blind zone, we only analyze the PBLH and CBH

300 above 0.2 km. Figure 5 4 presents the flow chart describing the updated DTDS

301 algorithm. In particular, we jointly use PBL development and the LCL to diagnose the

302 states of coupling or decoupling. In ideal situations, LCL, PBLH, and CBH are highly

303 consistent with each other for coupled clouds. But for real conditions, we only require

304 that either the LCL or the PBLH coincides with the CBH for identifying coupled cases,

305 with another parameter serving as an additional constraint. Specifically, a coupled cloud

306 needs to occur within a certain range of LCL and the previous position of the PBL top.

307   For the DTDS algorithm, five empirical parameters are used, including A_1, A_2,

308 A_3, A_4, A_5. As listed in the Table 1, $A_1 - A_5$ are set as 0.7, 0.2, 0.15, 1.35, and 1.1,

309 respectively. A cloud at time i is identified as being in the coupled state if the CBH is

310 less than $[H(i-1) + 0.2$ km $(A_2)]$ and [LCL$+0.7$ km $(A_1)]$. This step would

311 moves 39.5% of low cloud cases to the category of decoupled clouds. A cloud is also

312 considered to be in a coupled state if the CBH is coincident with the LCL within 0.15

313 km (A_3), and the CBH is less than $[H(i-1) + 0.7$ km $(A_1)]$, where $H(i-1)$

314 represents the PBLH at time $(i-1)$. This step would further moves 17.8% of the

315 remaining cases to the category of decoupled clouds.

316   The LCL is calculated from surface meteorological data (relative humidity,

317 temperature, pressure) at the SGP site based on an exact expression (Romps, 2017).

318 Sepcificly, Romps. (2017) proposed thean exact, explicit, analytic expression for LCL

319 as a function of surface meteorology. Compared to the previous approximate

320 expressions, some of which may have an uncertainty ofin the order of hundreds of

15

321 meters, ~~for which,~~ the Romps expression can be considered as the precise value. The

322 uncertainty of empirical vapor pressure data may lead to a bias of ~5-m (Romps, 2017),

323 which may be neglected in the analyses.

324 After determining the coupling or decoupling state of a cloud, we retrieve $H(i)$

325 (i.e., PBLH at time i) based on the cloud state. For decoupled cases, we use the same

326 strategy for a clear sky to retrieve the PBLH. Based on the selection scheme in the

327 DTDS algorithm, the LMP below the CBH is selected as $H(i)$. For coupled cases, we

328 jointly use CBH and CTH to determine PBLH. During the warm season, active cumulus

329 often occurs in the upper part of the PBL with strong surface heating, so the CBH can

330 be generally regarded as the PBLH (Stull, 1988; Wallace ~~&~~and Hobbs, 2006). Under

331 this condition, the CBH coincides with the previous PBL top. Therefore, if [CTH $\geq$

332 $PBLH_{30min} + 0.2\ km\ (A_2)]$, we set $H(i) = A_5 \text{CBH}$, where $PBLH_{30min}$ is the

333 average value of the PBLH within 30 min of the prior time i. Hence, A_5 would be a

334 critical parameter for the PBLH estimation. On the other hand, if [CTH $<$

335 $PBLH_{30min} + 0.2\ km\ (A_2)]$. we set $H(i)$ equal to the minimum between CTH and

336 the product A_4*CBH. This step is designed for thin clouds or some stratiform clouds.

337 In particular, A5-*-CBH can be notably larger than the CTH for a thin cloud. Under this

338 situation, we tend to use CTH to ~~represent~~denote the PBL top. This step has little impact

339 on the detection of surface-cloud coupling, but can assure that the CTH of the coupled

340 cloud is always higher than the retrieved PBLH to fit the real situation.

341 —After retrieving $H(i)$, we consider that the cloud above the PBLH is still coupled

342 if [CBH $<$ $H(i) + 0.2\ km\ (A_2)]$. Moreover, we added an upper limit for all PBLH

343   retrievals. If $[H(i) > \text{LCL} + 0.7 \ km \ (A_1)]$, we adjust $H(i)$ as the maximum LMP

344   below the LCL. The new DTDS method combines lidar measurements and surface

345   meteorological observations and can simultaneously retrieve the PBLH and cloud states.

346

347   *3.2.2 Selection of empirical parameters*

348   The states of coupling and decoupling are diagnostic parameters rather than explicit

349   expressions. Similar to the other methods for retrieving PBLH (e.g., Brooks, 2003; Liu

350   &and Liang, 2010), multiple empirical parameters are used to determine PBLH. Here

351   we discuss the selection of empirical parameters in the algorithm.

352   Note that we used the CTH and A_4*CBH as the upper limits for PBLH retrievals in

353   the DTDS algorithm. For coupled cases, these two limits are generally close to or above

354   the position of the PBL top. Only 2% (3%) of total cases meet the condition that the

355   RS-derived PBLH is 0.25 km higher than the CTH (A_4*CBH). Section 4 presents the

356   detailed relationships between CBH, CTH, and PBLH. In the DTDS method, CTH

357   serves as the upper limit for PBLH under the condition of coupled shallow cumulus.

358   Similar to previous studies, we can also use the LCL as the standard to identify

359   coupled clouds (Dong et al., 2015; Zheng &and Rosenfeld, 2015). We assume a cloud

360   is coupled if $|\text{CBH} - \text{LCL}| < \Delta h$ some criteria. By using ~7500 RS profiles, the cloud

361   coupling state derived from the virtual potential temperature method (Section 3.1) is

362   considered as the ground truth for evaluation. Figure 6a5a shows the commission errors

363   and omission errors for different criteria. Here, the commission error is calculated as

17

the percentage of decoupled clouds misidentified as coupled clouds. The commission error can also be called a "false positive", as the former is a common term for describing the nature of an error in identification. The omission error is calculated as the percentage of coupled clouds that have not been identified under this criterion. By using the LCL, we can obtain a relatively low commission error if the criterion is less than 0.15 km and a relatively low omission error if the criterion is greater than 0.7 km. Thus, we set A_1 and A_3 as 0.7 and 0.15 in the DTDS method to exclude and to select cases of coupled clouds. We can also use the RS-derived PBLH as the criterion (Figure 6b5b).

Despite the coarse temporal resolution, the RS-derived PBLH can be a good criterion to use to distinguish between coupling and decoupling. If we consider a coupled cloud as a cloud where (CBH < RS-derived PBLH + 0.2 km), both commission and omission errors are ~5%. Therefore, we primarily use [PBLH+0.2 km (A_2)] in the DTDS method to identify coupled and decoupled regimes. As cloud can considerably interfereaffect with lidar backscattering and generate large signal variations, we jointly use lidar backscatterings, the previous position of PBL top, and LCL to determine the surface-cloud coupling and PBLH. In particular, the LCL constraint in the algorithm notably reduces the absolute biases in PBLH retrievals under cloudy conditions by 9.3%.

Moreover, we test the sensitivity of selecting these empirical parameters. Figure 7 6 presents the commission errors and omission errors in the identifications of coupled clouds for selecting different values of empirical parameters. Among these parameters,

386   A_2 is the critical one, which would notably affect the identification results. In general,

387   A_2 determine the maximum differences between PBLH and CBH for coupled cases. If

388   [CBH-PBLH $> A_2$], we consider the cloud is under the decoupled state. Thus, the

389   identification method is quite sensitive to A_2. Selecting a low value of A_2 would

390   neglect many coupled cases, which leads to a high omission error. Meanwhile, selecting

391   a high value of A_2 would misclassify many coupled cases, which leads to a high

392   commission error. After a trail and error, A_2 is set as 0.2 km to balance the omission

393   and commission errors. The selections for other parameters are not sensitive for the

394   coupled cloud identifications. We can choose them from a reasonable range.

395   As a by-product of this method, we also pay attentions to the PBLH retrievals under

396   cloudy conditions. Figure 8 7 presents the mean absolute biases and correlation

397   coefficients between PBLH derived from lidar and radiosonde for selecting different

398   values of empirical parameters. To match the scope of this study, we only analyze the

399   low cloud conditions. For retrieving PBLH under cloudy conditions, A_2 is the critical

400   parameter. The variations in correlation coefficients under different values of empirical

401   parameters are small with a range of 0.81-0.82. However, the absolute biases can

402   considerably differ under different values of A_5. In general, A_5 represents the ratio

403   between CBH and PBLH under coupled conditions. If A_5 is above 1.1, PBLH

404   retrievals under cloudy conditions are overestimated. We set A_5 as 1.1 to achieve a

405   relatively low biasa relatively low biases and a relatively high correlation coefficient at

406   the same time. For other parameters, the selections from reasonable ranges would not

407   notably affect the PBLH retrievals.

In short, selections of these empirical parameters are based on the overall relationship between cloud and PBL under the coupled and decoupled states. In our method, the selection of A_2 is critical for the identifications of coupled clouds, while the selection of A_5 is critical for the PBLH retrievals under cloudy conditions. The selections of other parameters are not sensitive.

4　Results

Figure 9 Figure 8 illustrates four examples of PBLH retrievals and cloud states derived from the DTDS algorithm for 27 October 2011, 31 July 2002, 19 March 2000, and 1 May 2012. Figure 9a Figure 8a depicts coupled shallow cumulus occurring at noontime at the PBL top. With a weak surface flux of ~200 W m^{-2}, this shallow cumulus cloud appeared for less than an hour. Figure 9b 8b shows a developed coupled cumulus cloud. With a strong surface flux of ~500 W m^{-2}, this coupled cloud continuously developed during the daytime. Figure 9c 8c presents the case of a daylong coupled cloud. After the passage of a frontal system that day, stratocumulus occurred during the morning with a cloud thickness of 0.5 km. Through the development of the PBL, the thick stratocumulus cloud was broken up by the strong turbulences, transforming into shallow cumulus clouds. Figure 9d 8d shows the case of an active coupled cloud, which is generally associated with a large amount of convective available potential energy. Even though coupled clouds can differ in appearance and variability throughout the day, the common feature is the coherent variation between the cloud base and the PBL top.

20

429   The LCL is a relevant parameter and can differ from the PBLH and the CBH for some

430   coupled cases (e.g., Figure 9b8b-c).

431   The identification accuracy, or disparity between different methods, are evaluated

432   in terms of the selected criteria, for which the identification method based on $\Delta\theta_v$ is

433   regarded as the "truth", as described in Section 3.1. Hereafter, all results are analyzed

434   for the period of 1000–1900 LT, so early-morning data are not used. The commission

435   error is 10.1%, and the omission error is 6.8% for the DTDS method. Note that lidar-

436   based PBLH methods generally suffer from relatively low accuracy under stable

437   atmospheric conditions. Following Liu and Liang (2010), we identified stable PBLs

438   from RS measurements. Since coupled clouds are driven by relatively strong buoyancy

439   fluxes, only 1% of total cases of coupled clouds occurred under stable PBL conditions

440   during the study period (0700–1900 LT). Therefore, the relatively low accuracy for

441   stable PBLs is not a major problem in this study.

442   Figure 6 5 also compares the accuracy between the DTDS and LCL methods. Based

443   on the LCL alone, we cannot choose an appropriate criterion to achieve a lower

444   commission error and omission error simultaneously. Thus, we do not use the LCL as

445   the single standard to detect the coupling and decoupling of low clouds in our study. As

446   diagnostic parameters, different methods inevitably produce different results regarding

447   coupling and decoupling. Although we consider the method based on $\Delta\theta_v$ as the

448   standard, it still suffers from uncertainties arising from balloon drifting. From this

449   perspective, it is hard to conclude which method is best. Since it determines the

450   PBLH based on aerosol backscattering, the lidar-based method may be more

451 representative of the coupling between a cloud and the aerosol layer near the surface

452 when clear skies occur, at least during a short window of time.

453 Figure 10a9a-b presents the occurrence frequencies of the CBH and the CTH at

454 different heights. Despite the same variation ranges, clouds are mostly coupled if the

455 CBH is lower than 1 km, while decoupled clouds dominate if the CBH is higher than 3

456 km. Figure 10c9c-d shows the changes in the coupled fraction (ratio of coupled cases

457 to total cases) with different CBHs and CTHs. The coupled fraction is about 90% if the

458 CBH is lower than 1 km and decreases to 2% for CBHs above 3 km. Although the CBHs

459 for coupled cases are generally less than 3 km, CTHs for coupled cases can be much

460 higher. Coupled clouds still account for around 10% of the cases with CTHs above 6

461 km.

462 Figure 11 10 shows scatter plots between CBH, CTH, PBLH, and LCL for coupled

463 and decoupled clouds. For coupled clouds, there is a generally strong correlation

464 between CBH, LCL, and PBLH, contrary to the weak relationships of decoupled cases.

465 The relationship between CTH and RS-derived PBLH is complicated. For shallow

466 cumulus clouds, their tops can be considered as PBL tops for the coupled state, while

467 the cloud top is considerably above the position of the PBL top for active cumulus

468 clouds. We also note that the accuracy of CTH retrievals is generally lower than the

469 accuracy of CBH retrievals (Clothiaux et al., 2000). As CTH is not a criterion for cloud

470 coupling, the accuracy of CTH would not affect the identification of coupled cloud, but

471 may affect the PBLH retrievals for the coupled cloud cases. Meanwhile, despite the

472 laser-based detection of CBH is considered as the standard method (Platt et al., 1994;

22

473 Clothiaux et al., 2000; Lim et al., 2019), the CBH retrievals from ceilometer or lidar

474 still bear some uncertainties, which can potentially lead to a mean bias of 0.1km (Silber

475 et al., 2018; Cromwell et a., 2019). In our method, a systematic increase of 0.1 km in

476 the CBH can lead to an increase of 2.1% in omission errors and a decrease of 1% in

477 commission errors.

478 After identifying the coupling or decouplingstate of clouds, it is feasible to retrieve

479 the PBLH under cloudy conditionsthe PBLH can be successfully retrieved under cloudy

480 conditions. In particular, the DTDS-derived PBLH needs to resort to the cloud position

481 for coupled cloud cases. For decoupled cloud cases, on the other hand, the PBLH blow

482 clouds is sought to avoid cloud interference. For coupled clouds, DTDS-derived PBLHs

483 show a strong correlation with RS-derived PBLHs with a correlation coefficient (R) of

484 ~0.9 (Figure 10d). For decoupled cases, the correlation between DTDS-derived PBLHs

485 and RS-derived PBLHd is generally good (R = 0.73) but worse than the correlation for

486 coupled cases (Figure 10h). for atheAs pointed out in previous studies (Chu et al., 2019;

487 Hageli et al., 2000; Lewis et al., 2013; Su et al., 2017b), it has been a persistent problem

488 to retrieve the PBLH under cloudy conditions since the large strong backscattering and

489 step signals from cloud interference would be excluded to avoid interfering with the

490 retrievals. With our method, Tthe PBLH determined by our method under a cloudy

491 conditions demonstrates reasonably well accuracyis much more reasonable.

492 Compared to the clear-sky cases discussed in previous studies (e.g., Chu et al., 2019;

493 Yang et al., 2017), the DTDS-derived PBLH shows a much higher correlation with RS-

494 derived PBLH for coupled cloud cases and has a similar R as the RS-derived PBLH for

23

495 ~~decoupled cloud cases.~~ Moreover, due to the different definitions of the PBLH and

496 aerosol stratification within the PBL, there are always considerable differences between

497 lidar- and RS-derived PBLHs, which cannot be eliminated by a specific algorithm (Chu

498 et al., 2019; Su et al., 2020).

499

500 **5   Summary**

501   In this study, we proposed a novel method for distinguishing between coupled and

502 decoupled low clouds over land. Based on the understanding of PBL processes and

503 quantitative analyses, we developed a lidar-based method (DTDS) to identify the

504 coupling state of low clouds over the SGP site. In practice, we identified a coupled

505 cloud when the position of the cloud base was generally close to or lower than the

506 previous position of the PBL top, with the LCL serving as an additional restriction.

507 Compared to using the LCL alone, the coupled states identified by the DTDS method

508 show better consistency with the results derived from radiosondes, with about 10%

509 differences between the lidar-based retrievals and radiosonde results.

510   Not only coupled state, also retrieved by the method is the PBLH under cloudy

511 conditions. A long-lasting problem with lidar-retrieval of PBLH is either incapability

512 of retrieval or large uncertainties induced by the occurrence of low clouds (e.g., Chu et

513 al., 2019; Hageli et al., 2000; Lewis et al., 2013), we address this issue by separately

514 considering the coupled and decoupled of low clouds. Specifically, in coupled

515 conditions, the position of the coupled cloud serves as a good reference for identifying

516 the PBLH. In decoupled conditions, the large backscatter and step signals from clouds

24

517 would be excluded to avoid interfering with the retrievals. With our method, cloudy

518 conditions are well handled.

519   With the new method, we study the difference of cloud-PBL interactions in coupled

520 and decoupled conditions. In contrast to the sensitive responses of coupled clouds to

521 changes in the PBLH and buoyancy, the decoupled clouds and the PBLH are weakly

522 related. Due to their different relationships with the PBL, a robust distinguishment

523 between the coupled and decoupled low clouds is critical for further investigating the

524 coupled land-atmosphere system and aerosol-cloud interactions. Our methodology

525 paves a solid ground for such pursuits.

526

527 *Data availability.* All these datasets are publicly available at the ARM archive

528 https://adc.arm.gov/discovery/#/results/site_code::sgp. The products developed in this

529 study, i.e., cloud states and the PBLH, are currently available upon request from the

530 lead author (tianning@umd.edu) and are expected to be added to the ARM archive in

531 the near future.

532

533 *Author contribution.* T.S., Y.Z., and Z.L. conceptualized this study. T.S. carried out the

534 analysis, with comments from other co-authors. T.S., Y.Z., and Z.L. interpreted the data

535 and wrote the manuscript.

536

544

545 **References**

546 Berkes, F., Hoor, P., Bozem, H., Kunkel, D., Sprenger, M. and Henne, S. (2016).

547   Airborne observation of mixing across the entrainment zone during PARADE 2011.

548   Atmospheric Chemistry and Physics, 16(10), pp.6011-6025.

549 Betts, A.K. (2009). Land-surface-atmosphere coupling in observations and models.

550   *Journal of Advances in Modeling Earth Systems*, *1*(3).

551   https://doi.org/10.3894/JAMES.2009.1.4

552 Bretherton, C. S., &and Wyant, M. C. (1997). Moisture transport, lower-tropospheric

553   stability, and decoupling of cloud-topped boundary layers. *Journal of the*

554   *Atmospheric Sciences*, *54*(1), 148–167. https://doi.org/10.1175/1520-

555   0469(1997)054<0148:MTLTSA>2.0.CO;2

556 Brooks, I. M. (2003). Finding boundary layer top: application of a wavelet covariance

557   transform to lidar backscatter profiles. *Journal of Atmospheric and Oceanic*

558   *Technology*,   *20*,   1092–1105.   https://doi.org/10.1175/1520-

559   0426(2003)020<1092:FBLTAO>2.0.CO;2

560   Campbell, J. R., Hlavka, D. L., Welton, E. J., Flynn, C. J., Turner, D. D., Spinhirne, J.

561   D., …   Hwang, I. H. (2002). Full-time, eye-safe cloud and aerosol lidar

562   observation at atmospheric radiation measurement program sites: instruments and

563   data processing. *Journal of Atmospheric and Oceanic Technology*, *19*(4), 431–442.

564   https://doi.org/10.1175/1520-0426(2002)019<0431:FTESCA>2.0.CO;2

565   Campbell, J.R., Welton, E.J., Spinhirne, J.D., Ji, Q., Tsay, S.C., Piketh, S.J., Barenbrug,

566   M. and Holben, B.N., 2003. Micropulse lidar observations of tropospheric aerosols

567   over northeastern South Africa during the ARREX and SAFARI 2000 dry season

568   experiments. Journal of Geophysical Research: Atmospheres, 108(D13).

569   Cheruy, F., Dufresne, J. L., Hourdin, F., &and Ducharne, A. (2014). Role of clouds and

570   land-atmosphere coupling in midlatitude continental summer warm biases and

571   climate change amplification in CMIP5 simulations. *Geophysical Research Letters*,

572   *41*(18), 6493–6500. https://doi.org/10.1002/2014GL061145

573   Chu, Y., Li, J., Li, C., Tan, W., Su, T., &and Li, J. (2019). Seasonal and diurnal

574   variability of planetary boundary layer height in Beijing: intercomparison between

575   MPL   and   WRF   results.   *Atmospheric   Research*,   *227*,   1–13.

576   https://doi.org/10.1016/j.atmosres.2019.04.017

577   Clothiaux, E. E., Ackerman, T. P., Mace, G. G., Moran, K. P., Marchand, R. T., Miller,

M. A., &and Martner, B. E. (2000). Objective determination of cloud heights and radar reflectivities using a combination of active remote sensors at the ARM CART sites. *Journal of Applied Meteorology*, *39*(5), 645–665. https://doi.org/10.1175/1520-0450(2000)039<0645:ODOCHA>2.0.CO;2

Cromwell, E., and Flynn, D. (2019). Lidar cloud detection with fully convolutional networks. In 2019 IEEE Winter Conference on Applications of Computer Vision (WACV) (pp. 619-627). IEEE.

de Roode, S.R. and Wang, Q. (2007). Do stratocumulus clouds detrain? FIRE I data revisited. Boundary-layer meteorology, 122(2), pp.479-491.

Demoz, B., Flamant, C., Weckwerth, T., Whiteman, D., Evans, K., Fabry, F., …. &and Schwemmer, G. (2006). The dryline on 22 May 2002 during IHOP_2002: convective-scale measurements at the profiling site. *Monthly Weather Review*, *134*(1), 294–310. https://doi.org/10.1175/MWR3054.1

Dong, X., Schwantes, A. C., Xi, B., &and Wu, P. (2015). Investigation of the marine boundary layer cloud and CCN properties under coupled and decoupled conditions over the Azores. *Journal of Geophysical Research: Atmospheres*, *120*, 6179–6191. https://doi.org/10.1002/2014JD022939

Driedonks, A. G. M. (1982). Models and observations of the growth of the atmospheric boundary layer. *Boundary-Layer Meteorology*, *23*(3), 283–306. https://doi.org/10.1007/BF00121117

Ek, M. B., &and Holtslag, A. A. M. (2004). Influence of soil moisture on boundary

layer cloud development. *Journal of Hydrometeorology*, *5*(1), 86–99. https://doi.org/10.1175/1525-7541(2004)005<0086:IOSMOB>2.0.CO;2

Flynn, D., Shi, Y., Lim, K., &and Riihimaki, L. (2017). Cloud Type Classification (cldtype) Value-Added Product. Ed. by Robert Stafford, ARM Research Facility. DOE/SC-ARM-TR-200.

Garratt, J. R. (1994). Review: the atmospheric boundary layer. *Earth-Science Reviews*, *37*(1-2), 89–134. https://doi.org/10.1016/0012-8252(94)90026-4

Glenn, I. B., Feingold, G., Gristey, J. J., &and Yamaguchi, T. (2020). Quantification of the radiative effect of aerosol-cloud-interactions in shallow continental cumulus clouds. *Journal of the Atmospheric Sciences*, *77*, 2905–2920. https://doi.org/10.1175/JAS-D-19-0269.1

Golaz, J. C., Larson, V. E., &and Cotton, W. R. (2002). A PDF-based model for boundary layer clouds. Part I: Method and model description. *Journal of the Atmospheric Sciences*, *59*(24), 3540–3551. https://doi.org/10.1175/1520-0469(2002)059<3540:APBMFB>2.0.CO;2

Guo, J., Miao, Y., Zhang, Y., Liu, H., Li, Z., Zhang, W., … Zhai, P. (2016). The climatology of planetary boundary layer height in China derived from radiosonde and reanalysis data. *Atmospheric Chemistry and Physics*, *16*(20), 13,309–13,319. https://doi.org/10.5194/acp-16-13309-2016

Hageli, P., Steyn, D. G., &and Strawbridge, K. B. (2000). Spatial and temporal variability of mixed-layer depth and entrainment zone thickness. *Boundary-Layer*

620   *Meteorology, 97*, 47–71. https://doi.org/10.1023/A:1002790424133

621   Holdridge, D., Ritsche, M., Prell, J., ~~&~~and Coulter, R. (2011). Balloon-borne sounding

622   system (SONDE) handbook. https://www.arm.gov/capabilities/instruments/sonde

623   Holzworth, G. C., (1964). Estimates of mean maximum mixing depths in the contiguous

624   United States, Mon. Weather Rev., 92, 235–242, https://doi.org/10.1175/1520-

625   0493(1964)092<0235:eommmd>2.3.co;2.

626   Jones, C., Bretherton, C., ~~&~~and Leon, D. (2011). Coupled vs. decoupled boundary

627   layers in VOCALS-REx. *Atmospheric Chemistry and Physics*, *11*(14), 7143–7153.

628   https://doi.org/10.5194/acp-11-7143-2011

629   Kasahara, A. (1974). Various vertical coordinate systems used for numerical weather

630   prediction. *Monthly   Weather   Review*,   *102*(7),   509–522.

631   https://doi.org/10.1175/1520-0493(1974)102<0509:VVCSUF>2.0.CO;2

632   Lewis, J. R., Welton, E. J., Molod, A. M., ~~&~~and Joseph, E. (2013). Improved boundary

633   layer depth retrievals from MPLNET. *Journal of Geophysical Research:*

634   *Atmospheres*, *118*(17), 9870–9879. https://doi.org/10.1002/jgrd.50570

635   Lim, K.S.S., Riihimaki, L.D., Shi, Y., Flynn, D., Kleiss, J.M., Berg, L.K., Gustafson,

636   W.I., Zhang, Y. and Johnson, K.L. (2019). Long-term retrievals of cloud type and

637   fair-weather shallow cumulus events at the ARM SGP site. Journal of Atmospheric

638   and Oceanic Technology, 36(10), pp.2031-2043.

639   Liu, S. Y., ~~&~~and Liang, X. Z. (2010). Observed diurnal cycle climatology of planetary

boundary layer height. *Journal of Climate*, *23*, 5790–5809. https://doi.org/10.1175/2010JCLI3552.1

Lock, A. P., Brown, A. R., Bush, M. R., Martin, G. M., & Smith, R. N. B. (2000). A new boundary layer mixing scheme. Part I: Scheme description and single-column model tests. Monthly weather review, 128(9), 3187-3199.

Nicholls, S. (1984). The dynamics of stratocumulus: aircraft observations and comparisons with a mixed layer model. *Quarterly Journal of the Royal Meteorological Society*, *110*(466), 783–820. https://doi.org/10.1002/qj.49711046603

Ott, L. E., Bacmeister, J., Pawson, S., Pickering, K., Stenchikov, G., Suarez, M., ... and Xueref-Remy, I. (2009). Analysis of convective transport and parameter sensitivity in a single column version of the Goddard earth observation system, version 5, general circulation model. *Journal of the Atmospheric Sciences*, 66(3), 627-646.

Platt, C. M., Young, S. A., Carswell, A. I., Pal, S. R., McCormick, M. P., Winker, D. M., … &and Wooldridge, C. (1994). The Experimental Cloud LIdar Pilot Study (ECLIPS) for cloud-radiation research. *Bulletin of the American Meteorological Society*, *75*, 1635–1654. https://doi.org/10.1175/1520-0477(1994)075<1635:TECLPS>2.0.CO;2

Revercomb, H.E., Turner, D.D., Tobin, D.C., Knuteson, R.O., Feltz, W.F., Barnard, J., Bösenberg, J., Clough, S., Cook, D., Ferrare, R. and Goldsmith, J., 2003. The ARM program's water vapor intensive observation periods: Overview, initial

accomplishments, and future challenges. Bulletin of the American Meteorological Society, 84(2), pp.217-236.

Romps, D. M. (2017). Exact expression for the lifting condensation level. *Journal of the Atmospheric Sciences*, *74*(12), 3891–3900. https://doi.org/10.1175/JAS-D-17-0102.1

Santanello Jr., J. A., Dirmeyer, P. A., Ferguson, C. R., Findell, K. L., Tawfik, A. B., Berg, A., … &and Roundy, J. (2018). Land–atmosphere interactions: the LoCo perspective. *Bulletin of the American Meteorological Society*, *99*(6), 1253–1272. https://doi.org/10.1175/BAMS-D-17-0001.1

Sawyer, V., &and Li, Z. Q. (2013). Detection, variations and intercomparison of the planetary boundary layer depth from radiosonde, lidar and infrared spectrometer. *Atmospheric Environment*, *79*, 518–528. https://doi.org/10.1016/j.atmosenv.2013.07.019

Seidel, D. J., Ao, C. O., and Li, K. (2010). Estimating climatological planetary boundary layer heights from radiosonde observations: Comparison of methods and uncertainty analysis. Journal of Geophysical Research: Atmospheres, 115(D16).

Silber, I., J. Verlinde, E. W. Eloranta, C. J. Flynn, and D. M. Flynn (2018), Polar liquid cloud base detection algorithms for high spectral resolution or micropulse lidar data, J. Geophys. Res.: Atmos., doi: 10.1029/2017JD027840.

Storer, R.L., Griffin, B.M., Höft, J., Weber, J.K., Raut, E., Larson, V.E., Wang, M. and Rasch, P.J. (2015). Parameterizing deep convection using the assumed probability

32

density function method. Geoscientific Model Development, 8(1), pp.1-19.

Stull, R. B. (1988). *An Introduction to Boundary Layer Meteorology*. Dordrecht: Springer Netherlands.

Su, T., Li, J., Li, C. C., Xiang, P. Z., Lau, A. K. H., Guo, J. P., … ~~&~~and Miao, Y. C. (2017b). An intercomparison of long-term planetary boundary layer heights retrieved from CALIPSO, ground-based lidar, and radiosonde measurements over Hong Kong. *Journal of Geophysical Research: Atmospheres*, *122*, 3929–3943. https://doi.org/10.1002/2016JD025937

Su, T., Li, J., Li, J., Li, C., Chu, Y., Zhao, Y., … Wang, L. (2017a). The evolution of springtime water vapor over Beijing observed by a high dynamic Raman lidar system: case studies. *IEEE Journal of Selected Topics in Applied Earth Observations and Remote Sensing*, *10*(5), 1715–1726. https://doi.org/10.1109/JSTARS.2017.2653811

Su, T., Li, Z., ~~&~~and Kahn, R. (2018). Relationships between the planetary boundary layer height and surface pollutants derived from lidar observations over China: regional pattern and influencing factors. *Atmospheric Chemistry and Physics*, *18*(21), 15,921–15,935. https://doi.org/10.5194/acp-18-15921-2018

Su, T., Li, Z., ~~&~~and Kahn, R. (2020). A new method to retrieve the diurnal variability of planetary boundary layer height from lidar under different thermodynamic stability conditions. *Remote Sensing of Environment*, *237*, 111519. https://doi.org/10.1016/j.rse.2019.111519

703   Teixeira, J., &and Hogan, T. F. (2002). Boundary layer clouds in a global atmospheric

704   model: simple cloud cover parameterizations. *Journal of Climate*, *15*(11), 1261–

705   1276.   https://doi.org/10.1175/1520-

706   0442(2002)015<1261:BLCIAG>2.0.CO;Vogelezang, D. H. P., and Holtslag, A. A.

707   M. (1996). Evaluation and model impacts of alternative boundary-layer height

708   formulations. *Boundary-Layer   Meteorology*, *81*(3-4),   245–269.

709   https://doi.org/10.1007/BF02430331

710   Wallace, J. M., &and Hobbs, P. V. (2006). *Atmospheric Science: an Introductory Survey*.

711   Amsterdam, Boston: Elsevier Academic Press.

712   Warren, G., Hahn, C. J., London, J., Chervin, M., &and Jenne, R. L. (1986). Global

713   distribution of total cloud cover and cloud type amounts over land. (Rep. DOE/ER-

714   0406). Washington, DC: U.S. DOE Office of Energy Research.

715   Wei, J., Huang, W., Li, Z., Sun, L., Zhu, X., Yuan, Q., Liu, L. and Cribb, M., 2020.

716   Cloud detection for Landsat imagery by combining the random forest and

717   superpixels extracted via energy-driven sampling segmentation approaches.

718   Remote Sensing of Environment, 248, p.112005.

719   Welton, E. J., Campbell, J. R., Spinhirne, J. D., &and Scott III, V. S. (2001). Global

720   monitoring of clouds and aerosols using a network of micropulse lidar systems. In

721   *Lidar Remote Sensing for Industry and Environment Monitoring* (Vol. 4153, 151–

722   158). International Society for Optics and Photonics.

723   Wu, X., Grabowski, W. W, &and Moncrieff, M. W. (1998). Long-term behavior of cloud

34

systems in TOGA COARE and their interactions with radiative and surface processes. Part I: Two-dimensional modeling study. *Journal of the Atmospheric Sciences*, *55*(17), 2693–2714. https://doi.org/10.1175/1520-0469(1998)055<2693:LTBOCS>2.0.CO;2

Yang, D., Li, C., Lau, A. K. H., &and Li, Y. (2013). Long-term measurement of daytime atmospheric mixing layer height over Hong Kong. *Journal of Geophysical Research: Atmospheres*, *118*(5), 2422–2433. https://doi.org/10.1002/jgrd.50251

Yang, T., Wang, Z., Zhang, W., Gbaguidi, A., Sugimoto, N., Wang, X., Matsui, I. and Sun, Y., 2017. Boundary layer height determination from lidar for improving air pollution episode modeling: development of new algorithm and evaluation. Atmospheric Chemistry and Physics, 17(10), p.6215.

Zhao, C., Wang, Y., Wang, Q., Li, Z., Wang, Z., &and Liu, D. (2014). A new cloud and aerosol layer detection method based on micropulse lidar measurements. *Journal of Geophysical Research: Atmospheres*, *119*(11), 6788–6802. https://doi.org/10.1002/2014JD021760

Zheng, Y., &and Li, Z. (2019). Episodes of warm-air advection causing cloud-surface decoupling during the MARCUS. *Journal of Geophysical Research: Atmosphere*s, *124*(22). https://doi.org/10.1029/2019JD030835

Zheng, Y., &and Rosenfeld, D. (2015). Linear relation between convective cloud base height and updrafts and application to satellite retrievals. *Geophysical Research Letters*, *42*(15), 6485–6491. https://doi.org/10.1002/2015GL064809

745 Zheng, Y., Rosenfeld, D., &and Li, Z. (2018). Estimating the decoupling degree of

746   subtropical marine stratocumulus decks from satellite. *Geophysical Research*

747   *Letters*, *45*. https://doi.org/10.1029/2018GL078382

748 Zheng, Y., Sakradzija, M., Lee, S.-S., &and Li, Z. (2020). Theoretical understanding of

749   the linear relationship between convective updrafts and cloud-base height for

750   shallow cumulus clouds. Part II: Continental conditions. *Journal of the*

751   *Atmospheric Sciences*, *77*, 1313–1328. https://doi.org/10.1175/JAS-D-19-0301.1

752

Tables

Table 1. List of parameters in the flow chart of DTDS (Figure 54). These parameters are related with three factors, including LCL, PBLH, CBH. The sensitivity of selection of these parameters is presented. The detailed impacts of variations in these parameters on the retrievals of cloud coupling and PBLH are presented in Figure 76 and Figure 87, respectively.

	Unit	Related factors	Value	Sensitivity (coupled states)	Sensitivity 760 (PBLH)
A_1	km	LCL / PBLH	0.7	Low	Low
A_2	km	PBLH	0.2	**High**	Low
A_3	km	LCL	0.15	Low	Low
A_4	dimensionless	CBH	1.35	Low	Low
A_5	dimensionless	CBH	1.1	Low	**High**
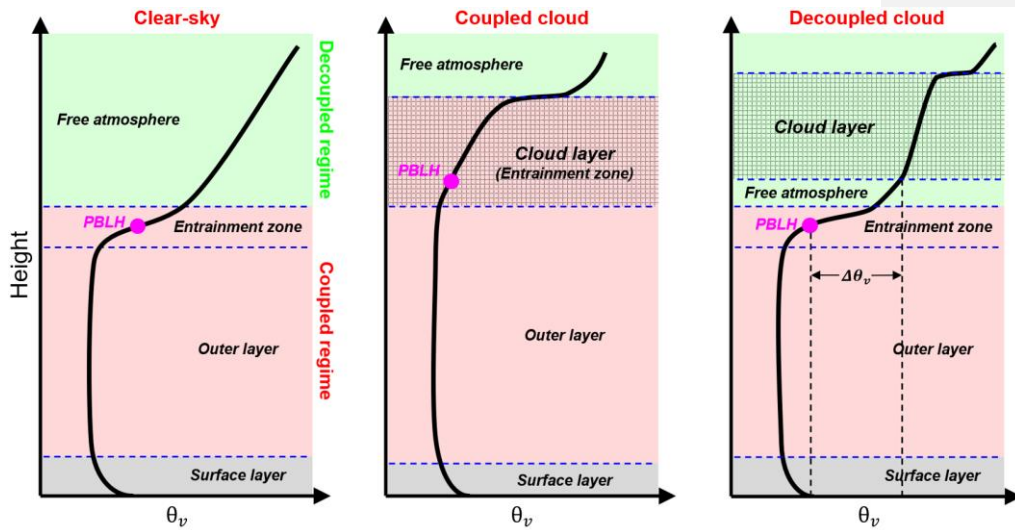
Figures

Figure 1. Idealized vertical profiles of virtual potential temperature (θ_v) under the clear-sky, coupled cloud, and decoupled cloud over land. The surface layer, outer layer entrainment zone, and free atmosphere are divided by the blue dash lines. The cloudy layer is marked as the shaded area, and PBLH is marked as the pink point. Red and green zones indicate the coupled and decoupled regime, respectively. Elements (e.g., turbulence, heat fluxes, cloud) in the coupled regime are directly affected by the PBL processes, while these elements are not directly affected by the PBL processes in the decoupled regime. For the coupled cases, the cloud base is below the capping inversion of entrainment zone. For the decoupled cases, the cloud base is above the capping inversion.

38
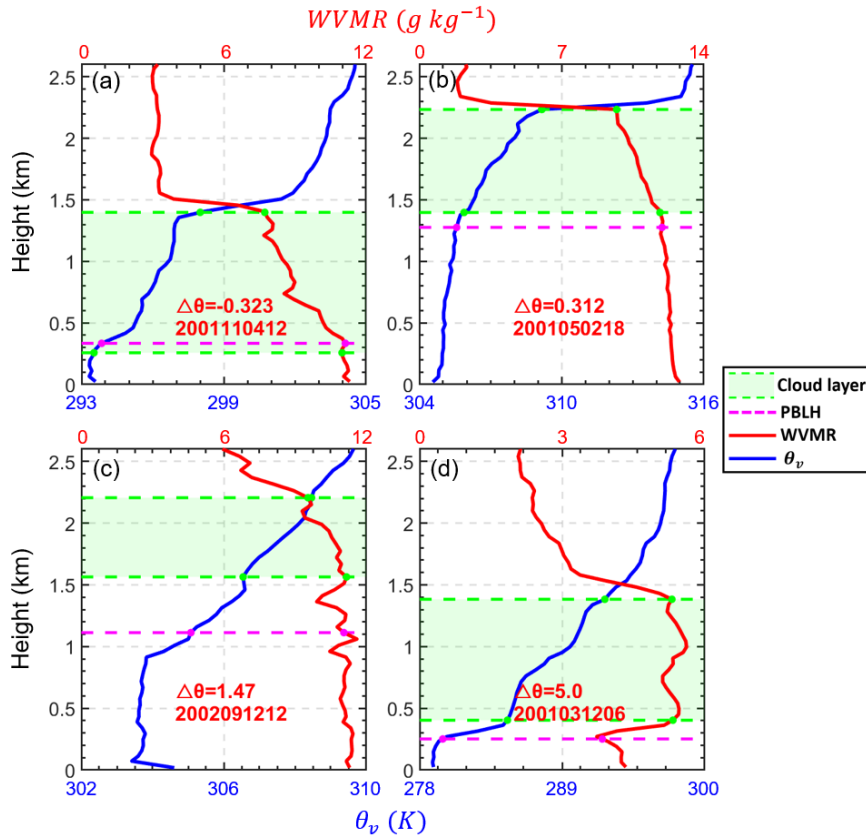
Figure 2. Virtual potential temperature (θ_v, red lines) and water vapor mixing ratio (WVMR, blue lines) profiles from radiosonde (RS) over the Southern Great Plains site for different cases. The differences in virtual potential temperature between the cloud base and the planetary boundary layer (PBL) top are expressed as $\Delta\theta_v$ ($\theta_v^{CBH} - \theta_v^{PBLH}$). The time of each radiosonde launch is marked in each panel as "YYYYMMDDHH", where YYYY, MM, DD, and HH indicates the year, month, day, and local time, respectively. Green regions are cloud layers, and green dashed lines indicate their boundaries. ~~PBL heights are~~The cloud layer is obtained from the

786
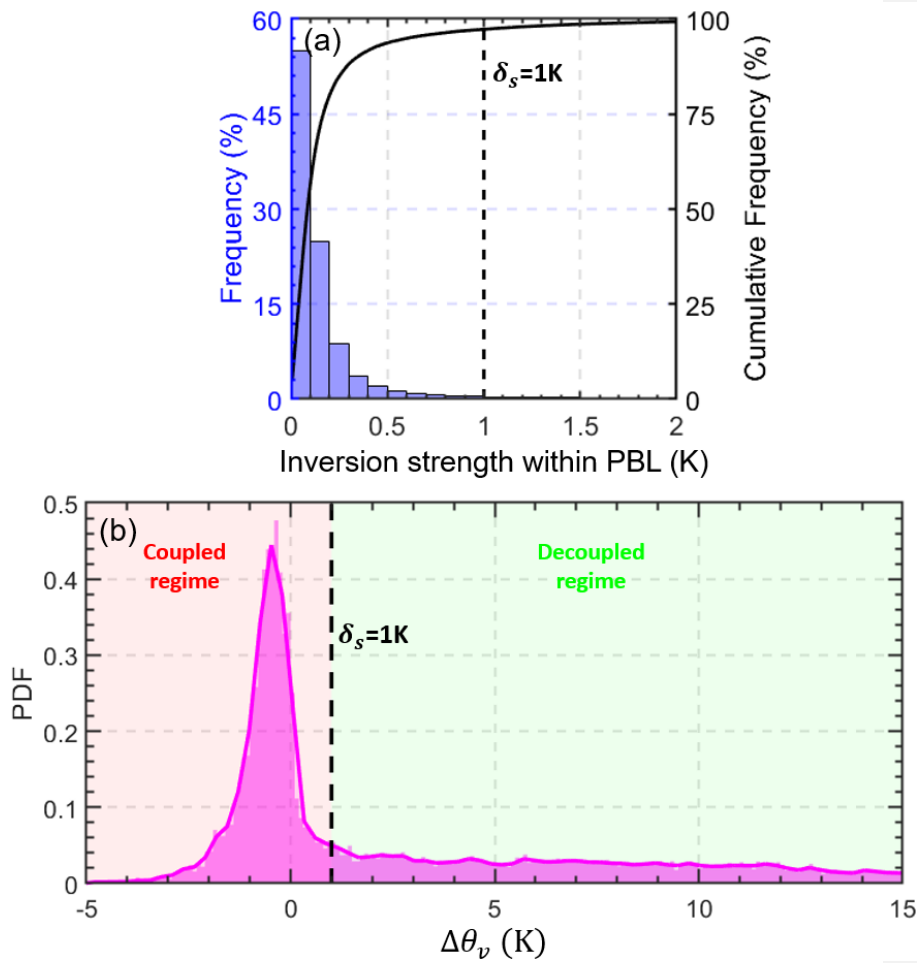
Figure 3. (a) Blue bars represent the inversion strength of θ_v within the PBL. The

inversion strength is derived from the radiosonde during daytime (0800-1900LT). The

inversions near surface or across PBL top are excluded. The black solid line represents

cumulative frequency. (b) Pink area represents the probability density function (PDF)

of the differences in the virtual potential temperature between cloud-base height (CBH)

792 and PBLH ($\Delta\theta_v = \theta_v^{CBH} - \theta_v^{PBLH}$). By using a threshold of δ_s (1 K), coupled and

793 decoupled regimes are classified.
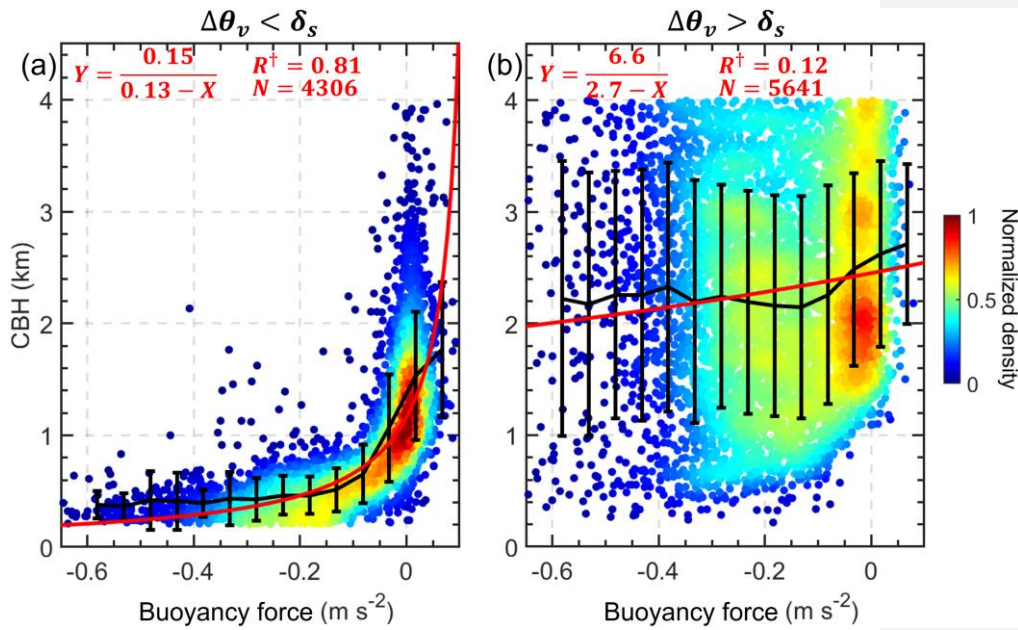
794

795 **Figure 4.** The relationships between cloud-base height (CBH) and buoyancy forces in

796 the lower atmosphere (0–1 km) for (a) $\Delta\theta_v < \delta_s$ and (b) $\Delta\theta_v > \delta_s$. $\Delta\theta_v$ represents the

797 differences in the virtual potential temperature (θ_v) between CBH and PBLH. Black

798 lines represent the mean values in each bin, and the whiskers indicate the standard

799 deviations. Red lines represent the inverse fits. The fitting functions and number of

800 samples (N) are given in each panel, along with the correlation coefficient ($R^{\ddagger}$) for the

801 inverse fit.
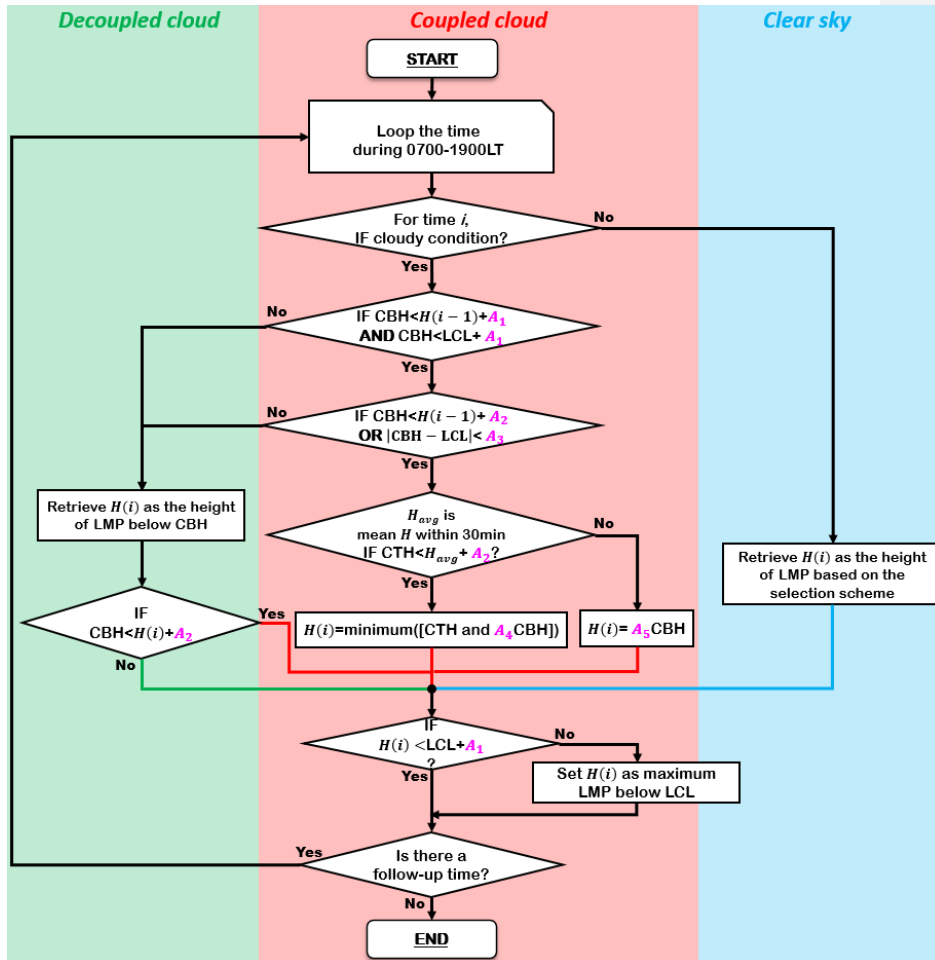
Figure 54. The flow chart of the updated DTDS algorithm. In this diagram, $H(i)$ is

the retrieved planetary boundary layer height (PBLH) at time i. CBH and CTH represent

the base and top heights, respectively, of the lowest cloud at time i. The PBLH part for

selecting the suitable local maximum position (LMP) follows Su et al. (2020), and a

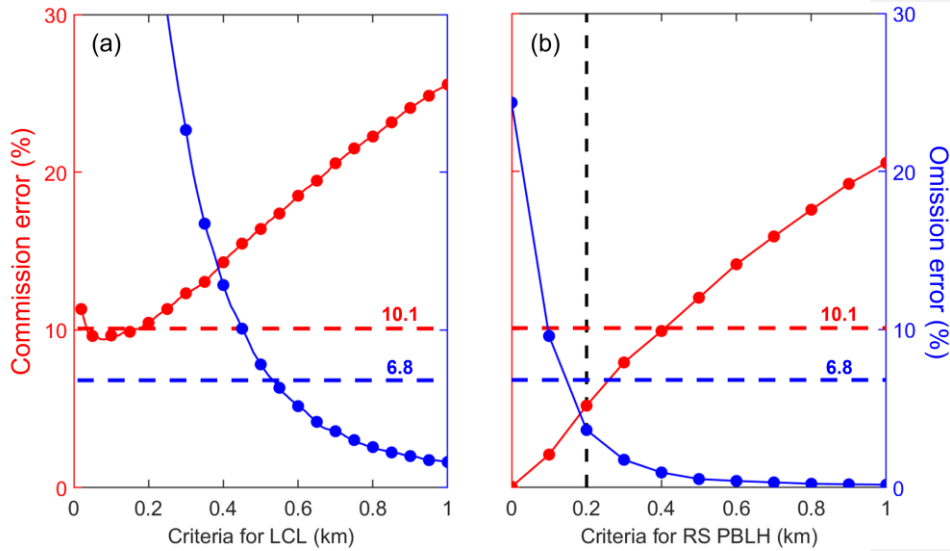detailed scheme for identifying a coupled cloud is added to the DTDS algorithm. LCL

stands for lifted condensation level. Five empirical parameters $(A_1, A_2, A_3, A_4, A_5)$ are

set as 0.7, 0.2, 0.15, 1.35, 1.1, respectively.

Figure 65. Commission errors and omission errors of coupled cloud identifications (a)

for different criteria for the lifted condensation level (LCL) and (b) for different criteria

for the planetary boundary layer height (PBLH). "Criteria for LCL" means coupled

clouds are identified if $|CBH - LCL| <$ Criteria for LCL. Similarly, "Criteria for RS

PBLH" means coupled clouds are identified if $CBH - $ RS PBLH $<$ Criteria for RS

PBLH. The red and blue dashed lines indicate the commission and omission errors,

respectively, for the DTDS algorithm. CBH stands for cloud-base height, and RS stands

for radiosonde. By using ~7500 RS profiles, the cloud coupling state derived from the

virtual potential temperature method (Section 3.1) is considered as the ground truth for

evaluation.

823

824

825
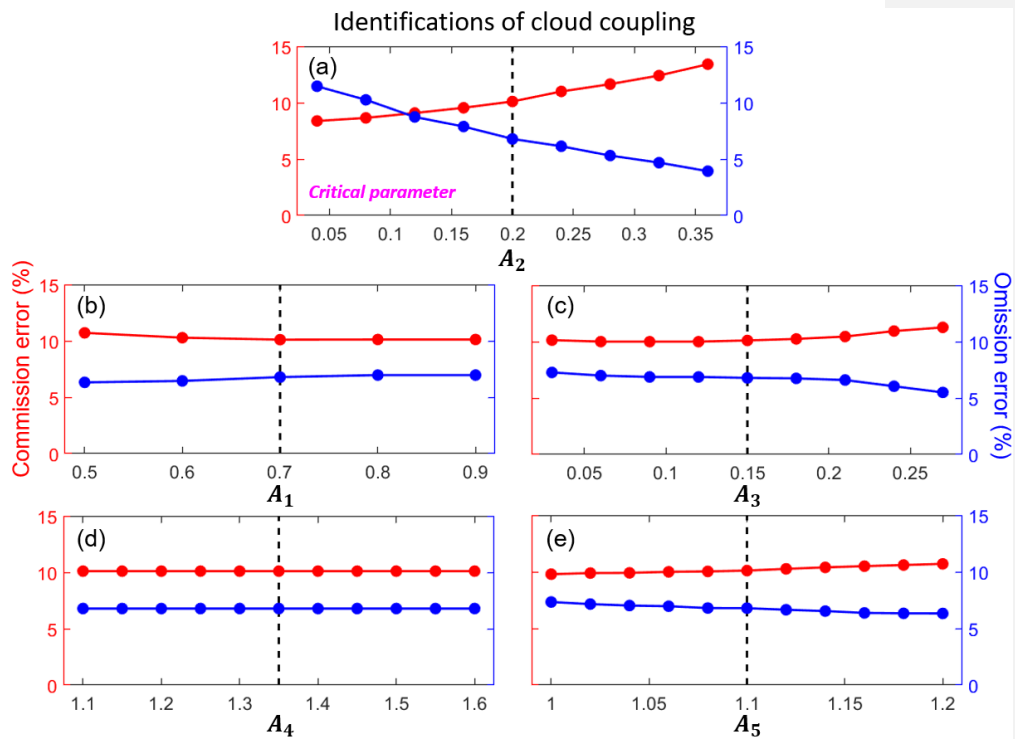
Figure ~~7~~6. Commission errors (red line) and omission errors (blue line) of coupled

cloud identifications for selecting different values of empirical parameters

$(A_1, A_2, A_3, A_4, A_5)$ in the DTDS algorithm. Black dash lines indicate the default values.

For each test, one parameter is variable, while other parameters are set as default values.

For identifications of cloud coupling, A_2 is the critical parameter.
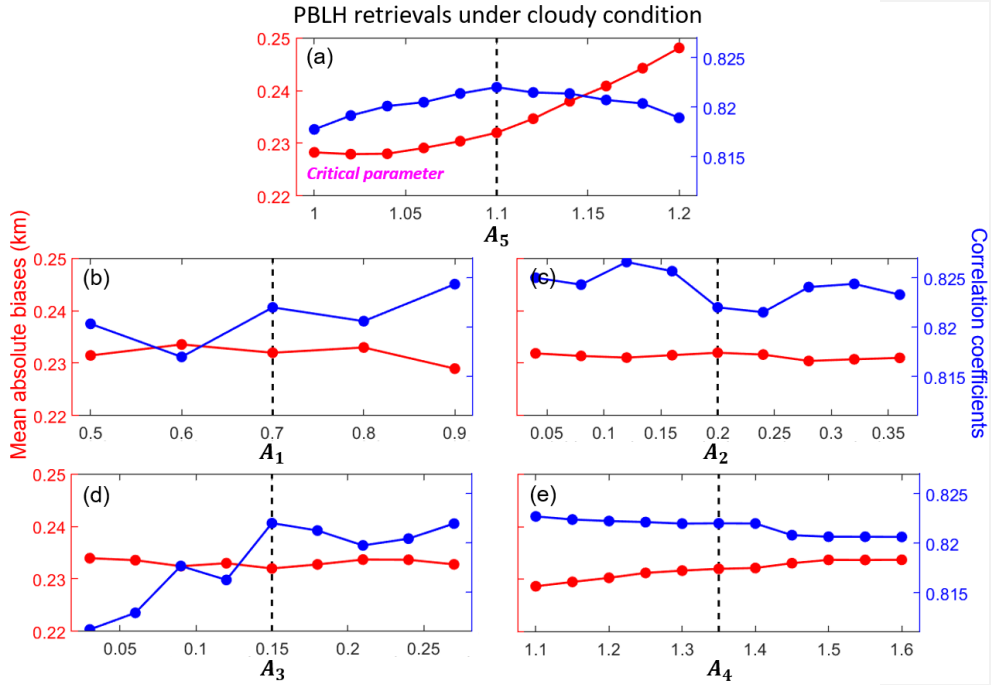
Figure 87. Red lines indicate the mean absolute biases between PBLH derived from lidar and radiosonde for selecting different values of empirical parameters $(A_1, A_2, A_3, A_4, A_5)$ in the DTDS algorithm. Here, we only analyze the low cloud cases. Blue lines indicate the corresponding correlation coefficients between PBLH derived from lidar and radiosonde. Black dash lines indicate the default values. For each test, one parameter is variable, while other parameters are set as default values. For PBLH retrievals under cloudy conditions, A_5 is the critical parameter.
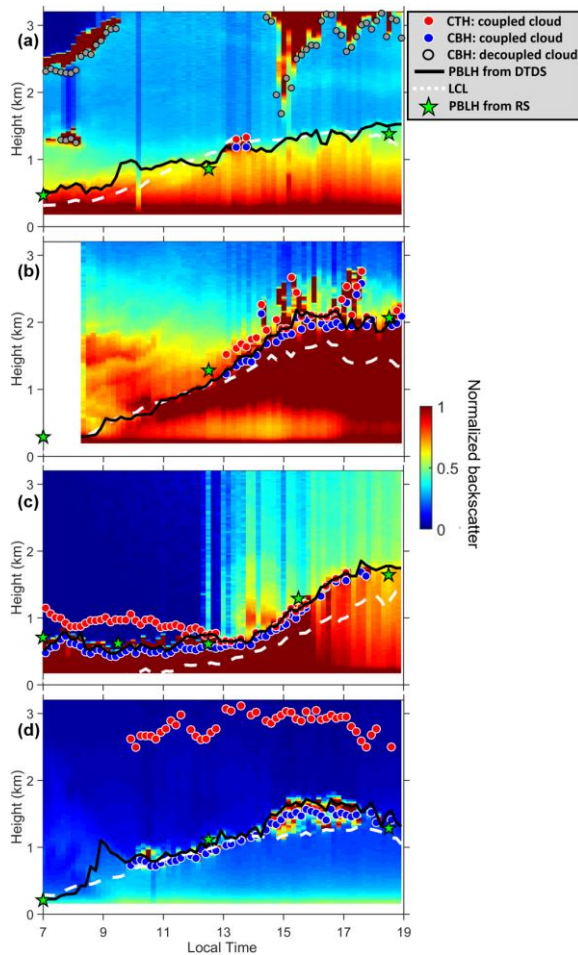
Figure 98. Daily backscatter profiles: (a) short-lived coupled cloud, (b) developed coupled cloud, (c) daylong coupled cloud, and (d) active coupled cloud. Backscatter is normalized to a range of 0–1 in arbitrary units. Red dots and blue dots indicate cloud-top heights (CTHs) and cloud-base heights (CBHs) of coupled clouds. Grey dots mark CBHs for decoupled clouds. Black lines and green stars mark the planetary boundary layer height (PBLH) retrieved from the DTDS algorithm and from radiosonde (RS) soundings, respectively. White dashed lines represent lifted condensation levels (LCLs).
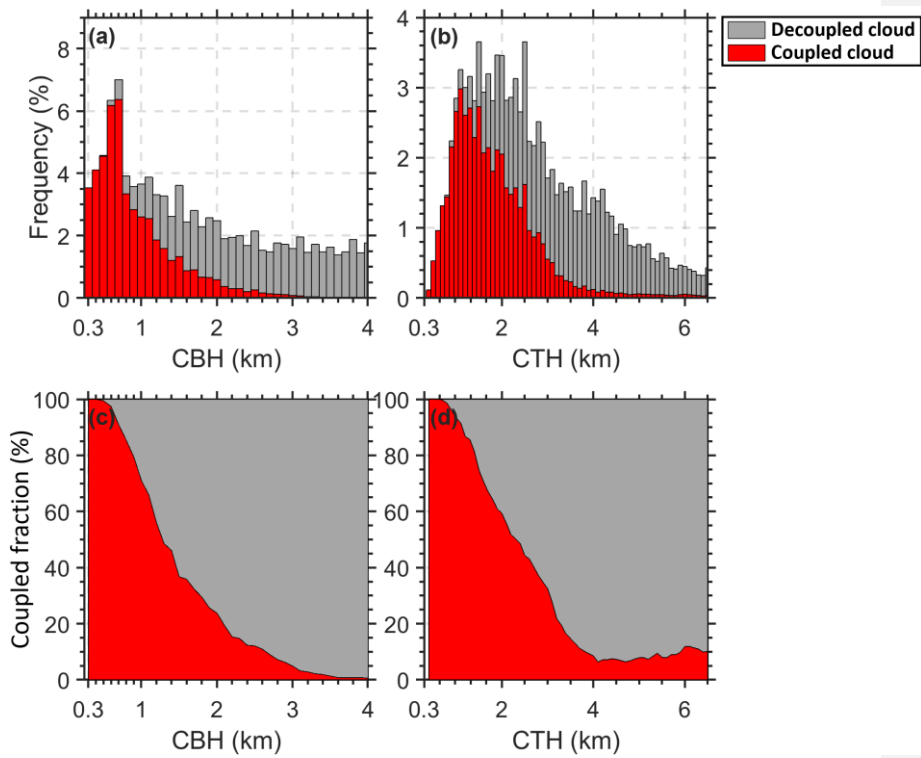
Figure ~~10~~9. The height-dependent occurrence frequencies of (a) the cloud-base height (CBH) and (b) the cloud-top height (CTH) for coupled clouds (red bars) and decoupled clouds (grey bars). The relative occurrence frequencies of (c) the CBH and (d) the CTH for coupled clouds (red area) and decoupled clouds (grey area).
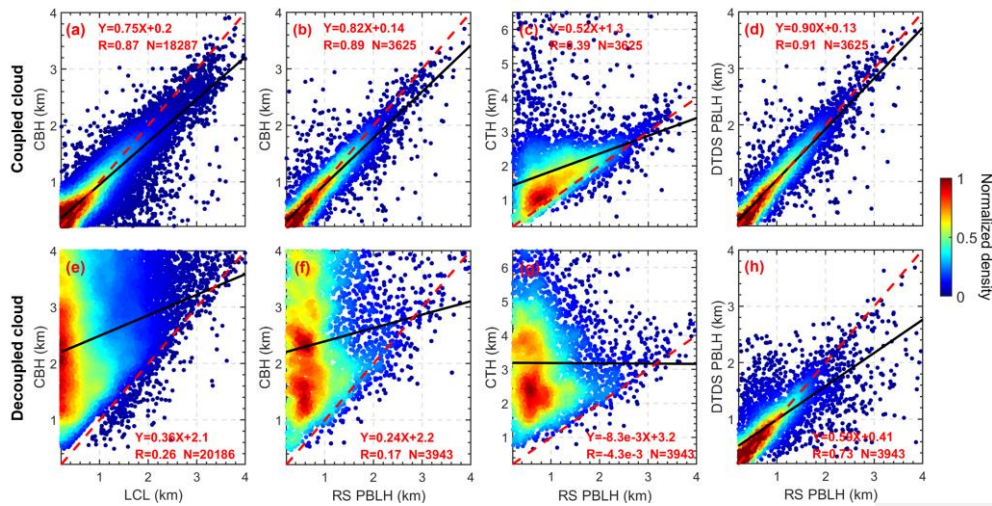
Figure ~~11~~10. The relationships between (a) LCL and CBH, (b) CBH and RS-derived PBLH, (c) CTH and RS-derived PBLH for coupled clouds, and (d) DTDS-derived PBLH and RS-derived PBLH. Panels (e-h) are similar to panels (a-d) but for decoupled clouds. Black lines represent the linear regressions. The linear fitting functions, correlation coefficients (R), and sampling numbers (N) are given in each panel.